Journal of The Electrochemical Society, **163** (5) C232-C239 (2016)
0013-4651/2016/163(5)/C232/8/$33.00 © The Electrochemical Society

Sigma and Random Grain Boundaries and Their Effect on the Corrosion of the Ni-Cr-Mo Alloy 22

N. Ebrahimi,[a] P. Jakupi,[a] A. Korinek,[b] I. Barker,[c] D. E. Moser,[c] and D. W. Shoesmith[a,*,z]

[a]*Department of Chemistry and Surface Science Western, University of Western Ontario, London, Ontario, Canada*
[b]*Canadian Centre for Electron Microscopy, McMaster University, Hamilton, Ontario, Canada*
[c]*Department of Earth Sciences, University of Western Ontario, London, Ontario, Canada*

The corrosion of the Ni-Cr-Mo alloy C22, has been studied in a simulated crevice corrosion environment (3 M NaCl + 1.5 M HCl at 75°C). Analyzing the corroded surface by electron backscatter diffraction showed that corrosion damage localized predominantly in random as opposed to Σ3 grain boundaries. Scanning transmission electron microscopy and electron energy loss spectroscopy showed that the susceptible random boundaries were decorated with needle-like inclusions enriched in O and depleted in Ni, suggesting a slight degree of internal oxidation during processing. The presence of line dislocations in the vicinity of the random boundaries may also have contributed to their corrosion susceptibility.

Manuscript submitted December 10, 2015; revised manuscript received February 1, 2016. Published February 17, 2016.

Nickel superalloys are a group of materials with excellent elevated-temperature strength, resistance to creep, and resistance to degradation in corrosive environments.[1,2] The Face Centered Cubic (FCC) structure of the γ phase of Ni, tolerates high alloying element solubility with Cr (35 wt%), Mo (20 wt%) and W (20 wt%).[3] Making extensive alloying possible without the formation of precipitates. These alloys are widely used in aerospace and power generation turbines, rocket engines and other challenging environments including chemical and petrochemical processing plants and oil and gas industry applications.[1,4] A key feature in their exceptional corrosion resistance is the ability to form a thin protective (passive) oxide film, which protects the underlying alloy,[5–7] and prevents failure by uniform corrosion in aggressive environments, but not necessarily localized corrosion processes such as pitting, intergranular corrosion and crevice corrosion.[8–13]

Recently, we have studied the propagation of crevice corrosion on a number of Ni-Cr-Mo alloys under controlled current conditions with the primary goal of determining those features which control the evolution and distribution of damage.[14–19] By investigating a series of alloys C22 (Cr22Mo13W3) and BC1 (Cr15Mo22), C2000 (Cr23Mo16Cu1.6) and Alloy 59 (Cr23Mo16)) it was shown that, while the macroscale distribution of corrosion damage on these alloys was predominantly controlled by the accumulation of molybdates at corroded locations the alloys all exhibited a pattern of intergranular attack with some grain boundaries being susceptible to corrosion while others remained undamaged. Jakupi et al.[20] showed that this pattern of intergranular corrosion, stimulated galvanostatically on C22 in 5.0 mol/L NaCl, propagated predominantly along randomly oriented rather than Σ3 boundaries.

Many material properties depend on the transmission of forces and stress fields across grain boundaries and are sensitive to the grain boundary structure, chemistry, and morphology.[21] Localized corrosion at grain boundaries is influenced by the 3-dimensional grain boundary structure, and reduced susceptibility to intergranular corrosion is associated with low energy grain boundaries.[22] The coincidence site lattice (CSL) model[23,24] is commonly used to describe the crystallographic relationship between the crystal lattices of adjacent grains. Each boundary is assigned a number, sigma (Σ), corresponding to the reciprocal number density of lattice sites that are common to both crystals. "Special boundaries" are characterized by a particular misorientation (Δθ), the difference in crystallographic orientation between two crystallites, and a high degree of atomic matching. They can be described geometrically by a low Σ number ($1 \leq \Sigma \leq 29$), with an allowable angular deviation from the Brandon criterion of $\Delta\theta \leq 15$ deg.[1] These boundaries possess extraordinary properties compared to high angle (>15°) "random" boundaries with $\Sigma \geq 29$.[20,23]

In recent years, grain boundary engineering (GBE), the deliberate manipulation of grain boundary structure, has been widely applied in the development of high performance structural and functional polycrystalline materials.[25–28] For FCC metals and alloys with low stacking fault energy, GBE has been used to generate a very high fraction of Σ3-related ($\Sigma = 3^n$) CSL boundaries coupled with the formation of annealing twins.[25] The generation of a structure with low Σ, CSL boundaries is thermodynamically favorable since they constitute a low energy configuration,[29] and many material properties are enhanced.

Kobayashi et al. found that high-energy random boundaries play a key role as the preferential crack path way during intergranular stress corrosion cracking with the crack length decreasing as the special boundary fraction increased.[25] Many other studies have observed that Σ, compared to random boundaries, are often more resistant to degradation reactions such as stress-corrosion cracking,[30,31] creep,[32] fatigue,[33] segregation and precipitation.[34]

While previous studies[20] established the greater susceptibility to intergranular attack of random, as opposed to Σ, grain-boundaries in the C22 alloy, the factors controlling the distribution of boundaries was unclear. In this study we have analyzed the grain boundary structures of alloy C22 (Table I) after immersion and corroding in acidic chloride solutions similar to those likely to be encountered in an active crevice. The electrode surface was characterized both before and after corrosion using electron backscatter diffraction (EBSD) and transmission electron microscopy (TEM) was performed on un-corroded sigma and random grain boundaries, with the primary goal of determining whether the distribution in Σ and random boundaries can be attributed to compositional differences.

Experimental

Materials and specimen preparation.—The chemical compositions of the alloy used in this study are given in Table I. Electrodes (1 cm^2 in surface area) were cut from as-received, mill-annealed bulk sheets supplied by Haynes International (Kokomo, IN, USA). The specimens were prepared for EBSD using the following procedure. Specimens were ground with a series of SiC papers (from 320 to 4000 grit) using water as a lubricant, and then polished on a Struers DP-Dur pad using a diamond paste (3 to 1 μm) as an abrasive. A final 0.05 μm polish was performed on a Struers OP-Chem pad using a solution mixture containing 50/50% ethylene glycol/0.05 μm

Table I. Alloy chemical compositions (wt%).

Alloying element	Ni	Cr	Mo	W	Fe	Co	C	Mn	S	Si
C22	56	22	13	3	3	2.5	0.01	0.5	0.02	0.08

*Electrochemical Society Fellow.
[z]E-mail: dwshoesm@uwo.ca

colloidal silica as an abrasive and ethylene glycol as a lubricant. The specimens were then sonicated in a 50/50% water/ethanol mixture for 5 minutes to remove any polishing residue. The polished surface was marked with a hardness indenter so that the characterized area could be relocated and reanalyzed after corrosion. SE (Secondary Electron) and BSE (Back Scatter Electron) images were recorded on the polished surface to identify any surface defects or polishing artefacts.

Electrochemical procedure.—For electrochemical measurements, a small hole was machined in the top of the specimens to connect to a cylindrical rod which provided a connection to external circuitry. A standard three-electrode, glass electrochemical cell was used for all experiments. The cell contained the specimen as the working electrode and a Pt counter electrode and saturated calomel (SCE) reference electrode (244 mV vs. SHE at 25°C). The cell had an outer jacket through which water was circulated from a thermostatic bath (Isotemp 3016H, Fisher Scientific) to maintain the temperature of the solution to within 1°C. In corrosion experiments, the specimen was exposed to a corrosive solution (3 M NaCl + 1.5 M HCl) for 8 hours at 75°C and the corrosion potential (E_{CORR}) recorded. Potentiodynamic polarization measurements were performed in the same solution at a scan rate of 0.5 mV/s. Before applying the scan, E_{CORR} was measured for 15 min to ensure a stable surface condition. Scans were started from a potential 50 mV below E_{CORR} and extended up to a value at which an abrupt increase in anodic current density occurred. All electrochemical measurements were conducted using a Solartron 1480 MultiStat, and Corrware software (Scribner and Associates).

Surface characterizations.—EBSD analyses were performed on specimens before and after corrosion in the ZAPlab laboratory at Western University. A Hitachi SU6600 field emission gun scanning electron microscope (FEG-SEM) operated at 20 kV was used to obtain grain orientation data. A step size of 1 μm was used to map the surface. HKL Channel 5 Tango software was used to obtain crystal orientation EBSD maps and electron backscatter patterns were indexed according to the FCC structure. Image-Pro Plus software was used to statistically analyze the corroded sites on grain boundaries and inside grains. A standard data clean-up or 'noise reduction' was performed on EBSD maps of un-corroded samples to remove points where indexing was not possible and to correct the points that have been incorrectly indexed using copies of the neighboring points.[35] However, no data cleaning was done on post corrosion EBSD maps.

The distribution of surface damage on the C22 alloy was imaged using an LSM 510 confocal laser scanning microscope (CLSM) in the Biotron facility at Western University. Samples for TEM analysis were prepared as follows. An orientation map obtained from EBSD of a finely polished un-corroded sample was used to identify a network of Σ (red) and random (yellow) grain boundaries, Figure 1a. Two adjacent Σ3 and random grain boundaries were then selected to avoid possible lateral differences in composition caused during solidification. A line across one of each type of boundary was then marked with Pt, Figure 1b, and a section cut out using a focused ion beam, Figure 1c. Finally, one of each type of boundary was thinned down for TEM analysis (Figure 1d). The FIB section was analyzed using a FEI Titan 80–300 microscope (FEI Company, Eindhoven, The Netherlands), equipped with a CEOS image corrector (CEOS GmbH, Heidelberg, Germany), an Oxford INCA x-sight system (Oxford Instruments, Abingdon, United Kingdom) and a Gatan Tridium energy filter (Gatan Inc., Pleasanton, CA). The microscope was operated at 300 kV.

Energy-dispersive X-ray spectroscopy (EDS) point analyses were performed in scanning transmission electron microscopy (STEM) mode, with a beam current of 150 pA and an acquisition time of 50 s. The dispersion per channel was 10 eV, and the process time was set to 4.

Electron energy loss spectroscopy (EELS) maps were acquired in STEM mode with a step size of 1.5 nm and an exposure time of 20 ms per pixel. The convergence semi-angle of the beam was set to 8 mrad. Diffraction patterns were acquired in STEM mode with a beam convergence semi-angle of 1 mrad and an exposure time of 100 ms. The illuminated area per diffraction pattern was approximately 2 nm. 2D maps of diffraction patterns were recorded in order to analyze the interface region.

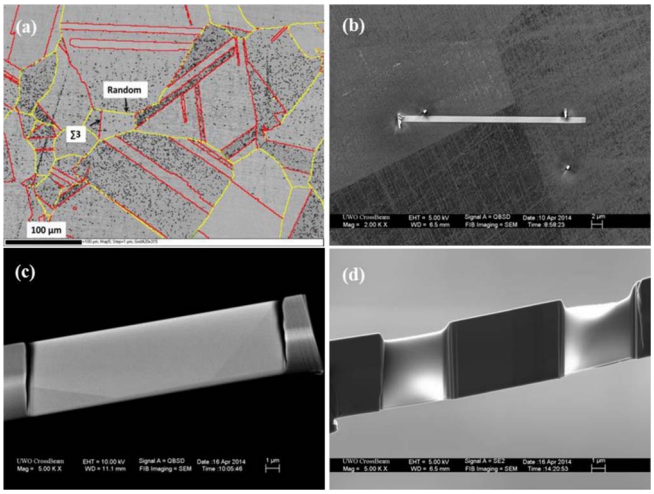

Figure 1. Preparation of a TEM sample using a focused ion beam. (a) sigma (red) and random (yellow) grain boundaries identified by EBSD: (b) selected Σ3 and random grain boundaries were chosen and marked with a line of Pt: (c) the cut specimen with the two grain boundaries at the two ends, (d) the final TEM specimen with thinned Σ and random boundaries.

Result and Discussion

Surface imaging of the un-corroded specimen.—After polishing the surface, areas of interests were selected and marked for analysis before and after corrosion. The Inverse Pole Figure (IPF) EBSD map of the analyzed surface is shown in Figure 2. The Σ and random grain boundary maps were superimposed on the IPF map in red and black, respectively. The percentage of Σ and random grain boundaries were calculated using Tango EBSD software and are presented with the corresponding IPF maps. C22 Alloy has a large number of Σ boundaries compared to random boundaries (69% Σ to 31% random) with a large number of the sigma boundaries (59%) as Σ3. Additionally, Annealing twins are well-developed in this alloy. The IPF maps show a wide distribution of crystallographic orientations with the C22 alloy exhibiting a preference for the {101} orientation.

The histogram of the grain size distribution is shown in Figure 3. A total of 220 grains were analyzed for C22 alloy, using Tango EBSD software to determine the size distribution. Estimation of grain size using EBSD is more precise than traditional methods, such as light microscopy of the etched surface, and allows twin boundaries to be disregarded in grain size estimations.[36] ASTM E112[37] is used for grain size measurement in this analysis. The histogram shows a large number of small grains and a decreasing number of grains as their size increases. The C22 alloy used in this study has relatively large grains with an average grain diameter of 42.8 μm with the maximum grain size detected to be 192.1 μm.

Corrosion and electrochemical measurements.—Figure 4 shows the potentiodynamic polarization curve recorded in the 3 M NaCl + 1.5 M HCl solution at 75°C. Consistent with the results of Lillard et al.,[38] the alloy exhibits an active region with a critical current (i_{crit}) value for the active to passive region of 2 mA/cm^2. Figure 5 shows that the E_{CORR}, recorded over a 7 h exposure period, initially decreases rapidly eventually achieving a steady-state value. The initial decrease can be attributed to dissolution of the native oxide film present on first immersion. The steady-state E_{CORR} value is −200 mV which is clearly in the active region (Figure 4) for C22 indicating this alloy would be

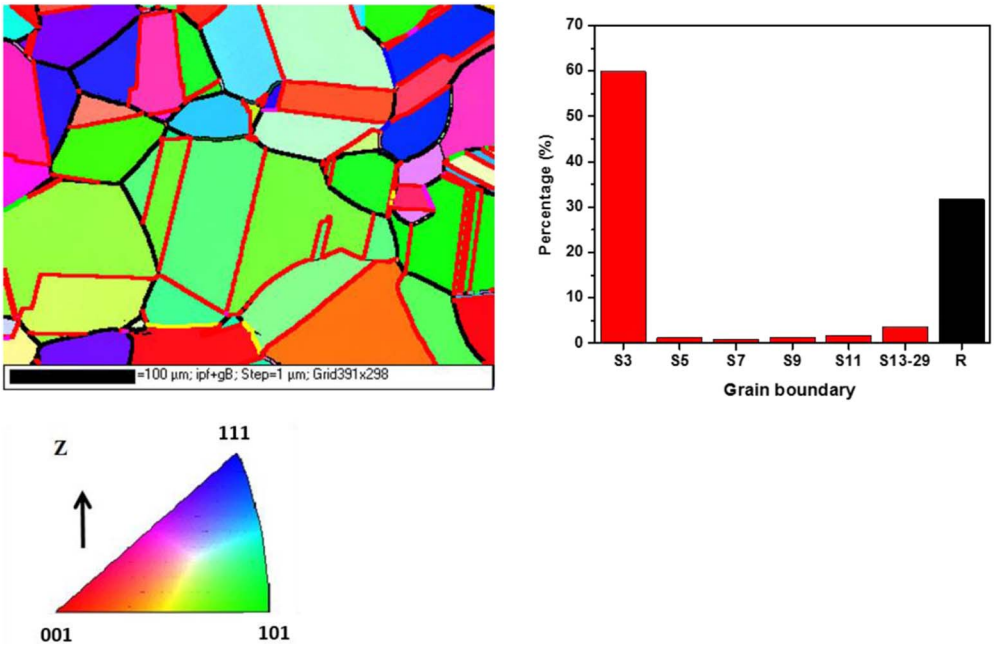

Figure 2. Crystallographic plane-normal orientation (IPF) maps for C22 alloys with Σ (red) and random (black) grain boundaries superimpose on the map. The accompanying graph shows the percentage of each type of boundary.

susceptible to crevice corrosion if the critical crevice solution achieved these acidic saline conditions. The E_{CORR} value is consistent with the values observed under active creviced conditions although the values are slightly less positive in this case in the absence of an applied current.[17]

Post-corrosion surface imaging.—A secondary Image (SE) micrograph of a selected area of the corroded surface is shown in Figure 6a. Corrosion was not extensive and the crystal orientations were maintained after corrosion. The most visible signs of corrosion are the intergranular trenches and the small etch pits on the grain surfaces. According to Horton and Scully,[39] based on a study of crystal orientation on the corrosion of FePd, which has a similar FCC structure to the alloys in this study, the corrosion rate is expected to be lowest on the three low index orientations of {111}, {100} and {110} and to increase when the grain orientation diverges from the {100} and {111} orientations.

An orientation map obtained by EBSD for the surface area shown in Figure 6a is presented in Figure 6b. Red and yellow lines indicate Σ and random grain boundaries, respectively, with non-indexable locations shown in green. The inability to index certain sites can be attributed to corrosion as clearly indicated by the correlation between their location in the map with the etch pits on the grain surface shown in Figure 6a.

As clearly observable in Figure 7a, and in the corresponding EBSD map in Figure 7c, some grain boundaries are corroded while others are not. In addition many of the triple point junctions are also preferentially corroded, Figure 7b. Close inspection (Figure 7d), enabled the characterization of four distinct groups of triple point junctions: junctions linking three Σ boundaries (ΣΣΣ), two ΣΣ and one random boundary (ΣΣR), one Σ and 2 random boundaries (ΣRR), and three random boundaries (RRR), for which the last type proved

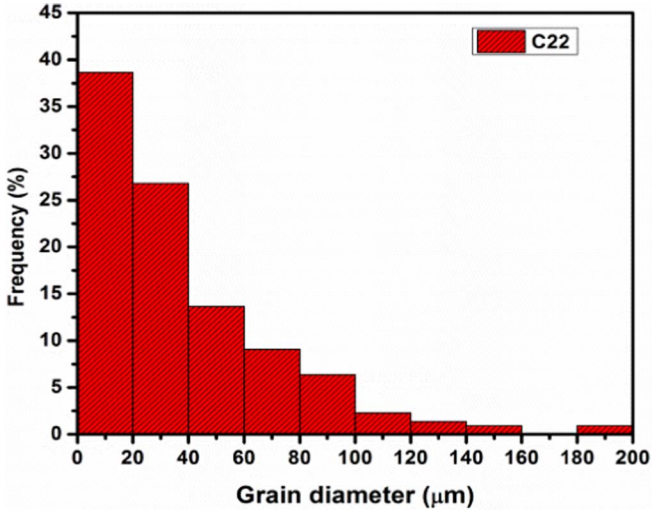

Figure 3. Grain diameter distributions for the C22 alloy.

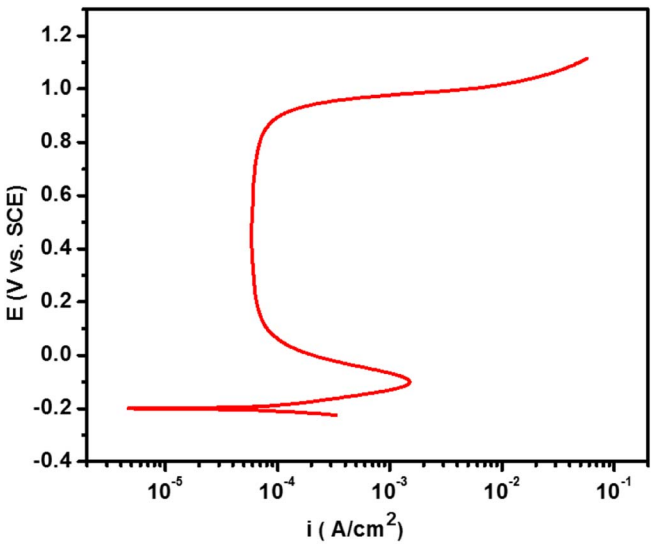

Figure 4. Potentiodynamic polarization curve for the C22 alloy in 3 M NaCl + 1.5 M HCl at 75°C solution at a scan rate of 0.5 mV/s.

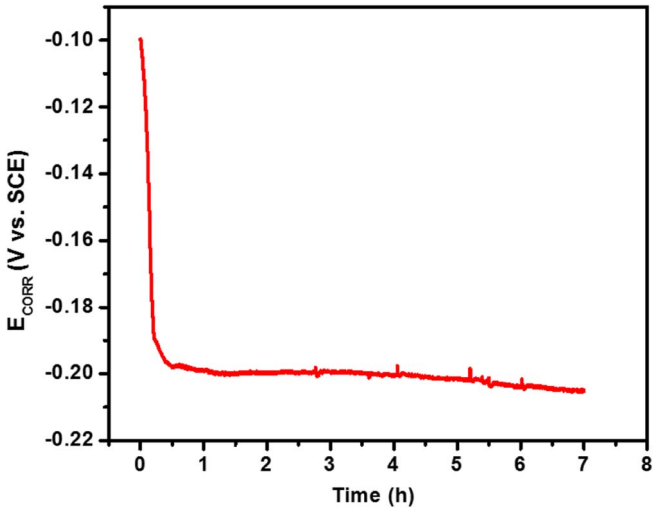

Figure 5. Corrosion potential (E_{CORR}) recorded on the C22 alloy over a 7 hour immersion period in 3 M NaCl + 1.5 M HCl at 75°C.

most susceptible to corrosion. A statistical analysis was performed to compare the corrosion resistance of Σ and random boundaries. All grain boundaries (a total of 156) of the pre-corrosion analyzed map was analyzed. The length of all the Σ and random boundaries, and also the length of corroded regions on each type of grain boundary were measured using Image Pro software. The fraction of Σ and random grain boundary length (%) corroded was calculated as the ratio of the corroded length over the total length of each characterized boundary (Figure 8). These calculations show the Σ boundaries were considerably more resistant than the random boundaries: 16% (random) and 1.7% (Σ). These results are consistent with previous observations.[20]

Confocal laser microscopy of C22 corroded grains.—Besides intergranular corrosion and grain defect etching the alloys also exhibited different rates of grain surface dissolution depending on the crystallographic orientation of the grain. The corroded specimen was investigated using CLSM. Figure 9 shows 3D CLSM images of the areas circled in the inverse pole figure maps. These images show that the corrosion rates of individual grains correlates with their orientation in the surface normal direction.

The intergranular corrosion can be seen in Figures 9c and 9d, and closer observation of individual grains shows that some grains are high relative to adjacent neighbors, the difference in height being due to general corrosion. The dissolution behavior of the grains was found to correlate with their orientation in the surface normal direction. The majority of high grains are blue on the EBSD map meaning they exhibit a {111} orientation. These grains oxidize at a slower rate and are more corrosion resistant than grains in other orientations. This is the most densely packed plane with the lowest relative energy in the FCC crystal lattice and would be expected to have the slowest

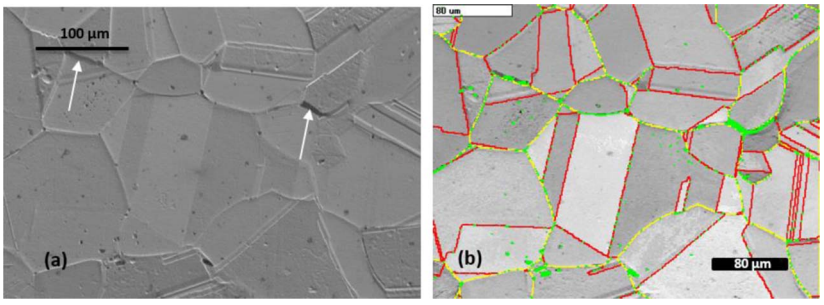

Figure 6. (a) SE image of the C22 surface after exposure to the acidic solution, arrows shows some of the intergranular trenches: (b) the corresponding orientation map superimposed on the image. All Σ and random grain boundaries are in red and yellow, respectively. Non-indexed points (mostly due to localized corrosion) are in green.

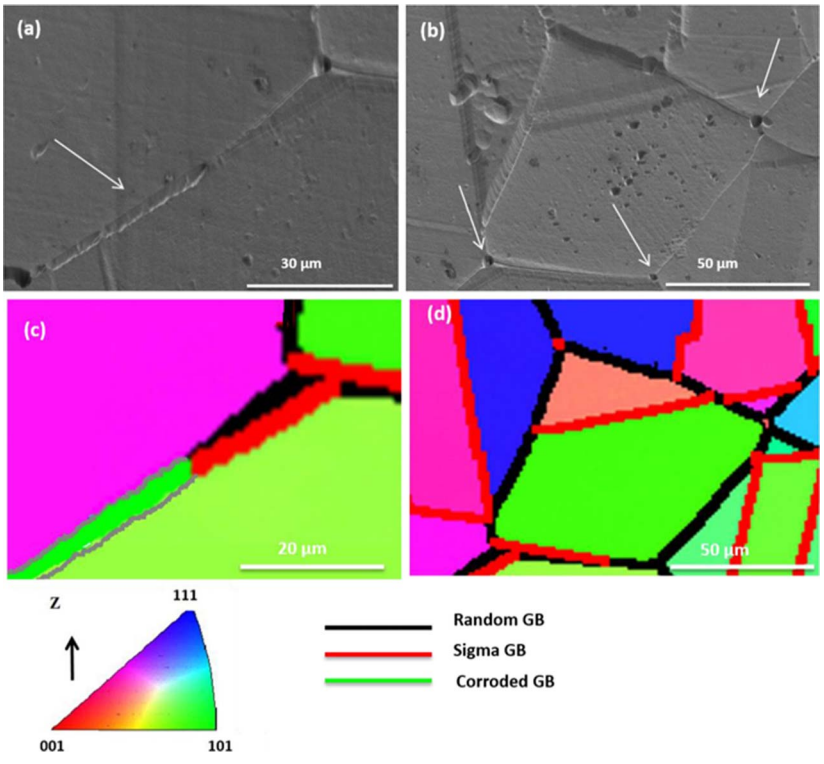

Figure 7. (a) A corroded random grain boundary: (b) corroded triple points in the C22 alloy. (c) and (d) the corresponding orientation map superimposed on the inverse pole figure map for region (a) and (b), respectively.

corrosion rate, Gray et al.[40] having reported that the corrosion rate of C22 decreases with the plane normal crystallographic orientation in the order $\{111\}, \{110\} < \{100\}$.

TEM analysis.—To investigate the reasons for the enhanced corrosion resistance of Σ boundaries, TEM specimens were prepared from a Σ and a random grain boundary. The specimens, cut with a focused ion beam, were characterized using a scanning transmission electron microscope (STEM) equipped with an electron energy dispersive X-ray analyzer (EDS). The EDS analyses were performed at a number of locations across the boundaries, as indicated in Figure 10.

Figure 11 summarizes the compositions obtained from this analysis and shows uniform composition on both sides of the boundary, the location of which is indicated by the dashed line. No significant change in elemental composition is observed across either grain boundary. Table II shows the mean, minimum and maximum and standard deviation of the EDS data points across the Σ and random grain boundaries. The homogeneity in composition is demonstrated by the small standard deviation (<0.6%). Due to the weak detection limit for EDS these minor differences are not significant.

The boundaries were also examined by Annular Dark Field (ADF) STEM. Bright needle inclusions were detected in random boundaries in close proximity to the grain boundary and protruding into the grain, Figure 12b. The length of these inclusions was ∼20 to 40 nm. No similar inclusions were detected on the Σ boundaries, Figure 12a. Subsequently, EELS analysis was performed to investigate the nature of these inclusions.

ADF-STEM micrographs of the regions on either side of the grain boundaries are shown in Figure 13 along with the corresponding EELS maps for the same locations. For the random boundary the inclusions detected in the ADF STEM images are shown to be depleted in Ni and slightly enriched in O however, no changes in Fe and Cr content were detected. For the Σ boundary no Ni depletion/O enrichment was observed, all elements (O, Ni, Fe, Cr) being uniformly distributed within both grains and along the grain boundary. No Mo EELS map could be obtained by this method since the specimen thickness was too large and thus the signal background generated by multiple scattering events was higher than the anticipated Mo peak at the given Mo concentration. A possible explanation for the depletion of Ni/enrichment of O in the random boundary is a slight degree of internal oxidation during alloy processing. This is not uncommon in Cr-containing Ni alloys in high temperature applications due to the affinity of Cr to oxidation leading to the expulsion of Ni from that location.[41–43]

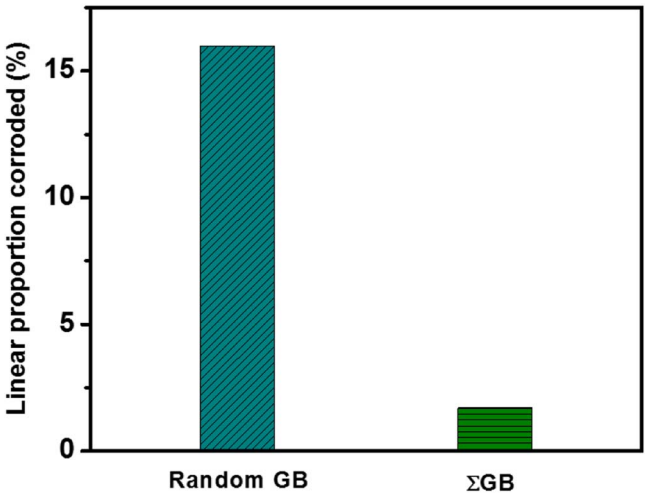

Figure 8. Fraction of Σ and random grain-boundaries that underwent corrosion.

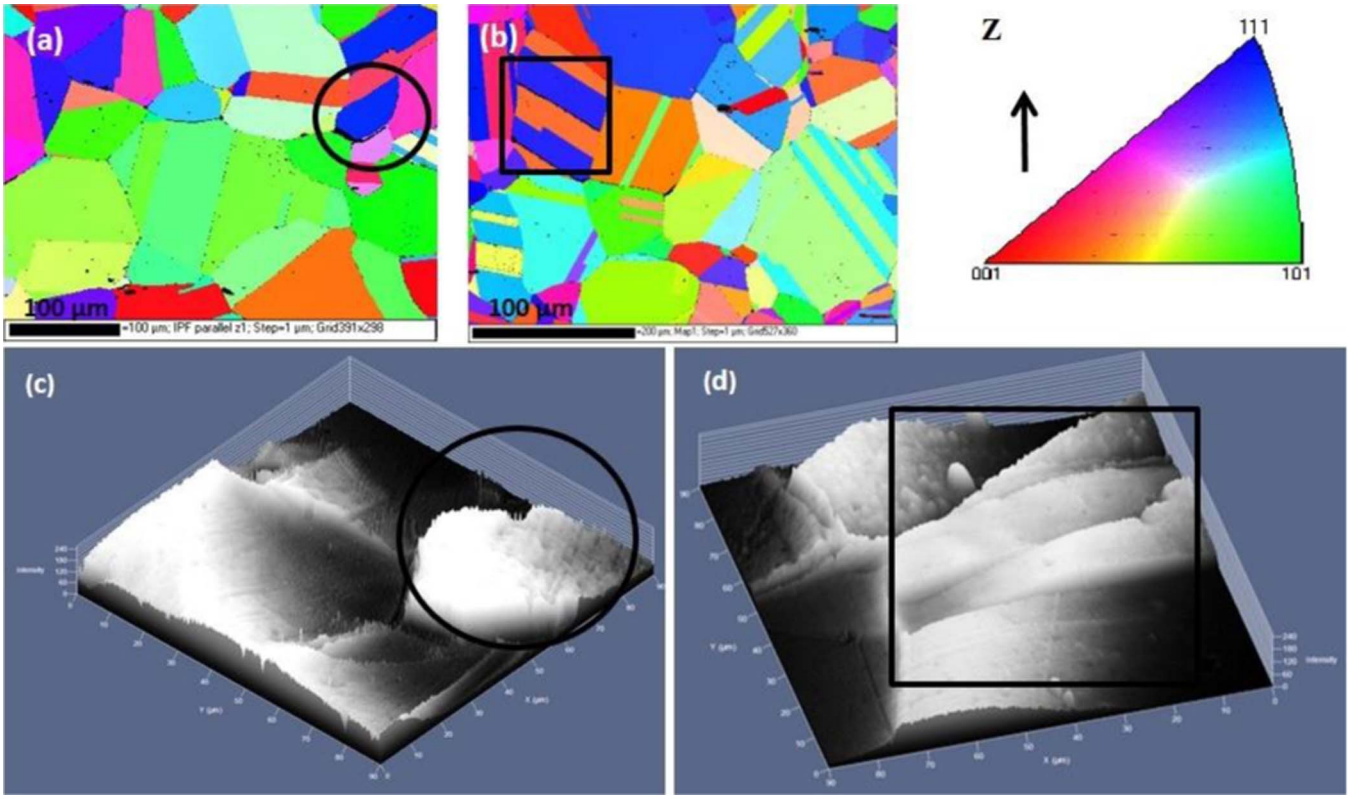

Figure 9. Inverse Pole Figure (IPF) maps (a) and (b) and Confocal Laser Microscopy images (c) and (d) of the corroded C22 sample. The marked grains in maps (a) and (b) are shown in the images (c) and (d).

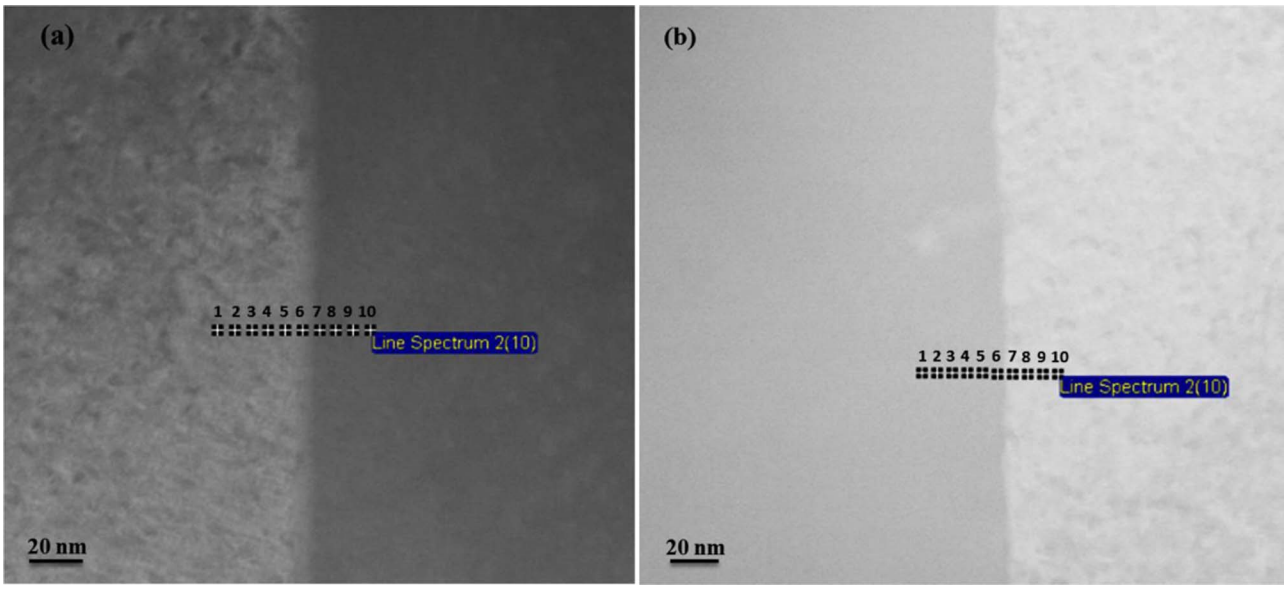

Figure 10. EDS data points (1 to 10) recorded on the TEM sample across (a) a Σ and (b) a random grain boundary (Figure 10).

The diffraction patterns recorded in the same regions were analyzed for both grain-boundaries, Figure 14. The transition in diffraction pattern from one grain to the other is abrupt for a random boundary, as expected for the high degree of mismatch between the orientations in the two grains. Analysis of the diffraction patterns recorded in adjacent grains, confirms the nature of these inclusions is different from that of other locations in the grain-boundary, although their identity remains to be confirmed. In contrast, the Σ3 grain boundary shows no distinct diffraction peaks, the interface between the grains yielding the sum of the diffraction patterns of both grains. This is not surprising since the chosen grain boundary is a Σ3 boundary with one in each three lattice points coincident within the boundary.

Figure 15 shows the line dislocations detected in the vicinity of random grain boundaries, with close inspection of Σ3 boundaries not revealing similar features. This observation is in agreement with recent experimental[44] and computational studies[45] on the distribution of relative grain boundary energies in Ni. Li et al.[44] showed that Σ3 boundaries have lower energies than others and therefore, the accumulation of dislocations near a higher energy random boundary is not unexpected. The higher corrosion resistance of Σ3 could be also due to the lower density of dislocations at these sites.

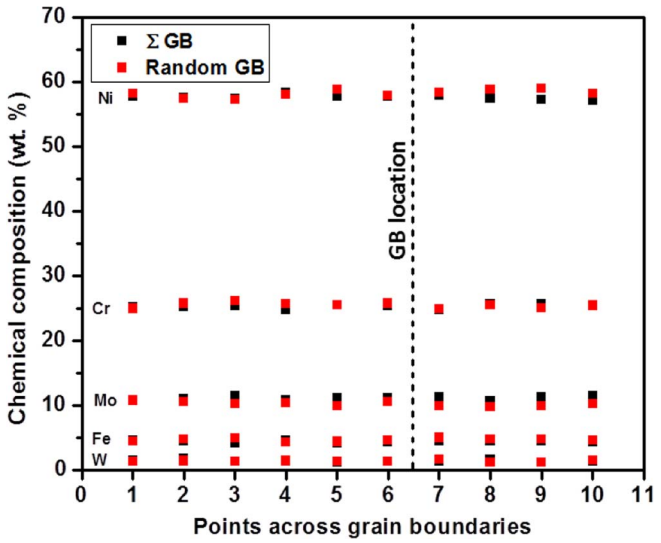

Figure 11. Elemental composition (wt%) at the numbered locations across a Σ and a random grain-boundary (Figure 10).

Conclusions

EBSD analyses of the Ni-Cr-Mo alloy C22 showed that it corroded preferentially in the grain boundaries with the majority of the damage occurring on random, as opposed to Σ3, boundaries.

While EDS analyses performed across grain boundaries detected no measurable compositional differences, STEM analyses did detect needle-like inclusions on the random but not the Σ3 boundaries.

EELS analyses showed these inclusions were enriched in O and depleted in Ni indicating a slight degree of internal oxidation occurred during processing. While confirming the mismatch in orientation between randomly oriented adjacent grain boundaries diffraction patterns did not identify the nature of the inclusions.

The presence of line dislocations in the vicinity of random grain boundaries could also contribute to their enhanced susceptibility to corrosion.

This study confirms that the nature of the grain boundaries has a significant influence on the damage pattern.

Table II. The mean, minimum, maximum and standard deviation of the EDS data points measured across Σ and random grain boundaries.

	Sigma Boundary					Random Boundary				
Elements/Points	Ni	Cr	Mo	Fe	W	Ni	Cr	Mo	Fe	W
Mean	57.7	25.3	11.2	4.4	1.4	58.2	25.5	10.2	4.6	1.3
Std. Dev.	0.3	0.3	0.3	0.2	0.2	0.6	0.4	0.3	0.2	0.1
Min	57.2	24.8	10.7	4.2	1.1	57.3	24.9	9.8	4.3	1.2
Max	58.4	25.7	11.5	4.6	1.7	59.0	26.2	10.8	5.0	1.6

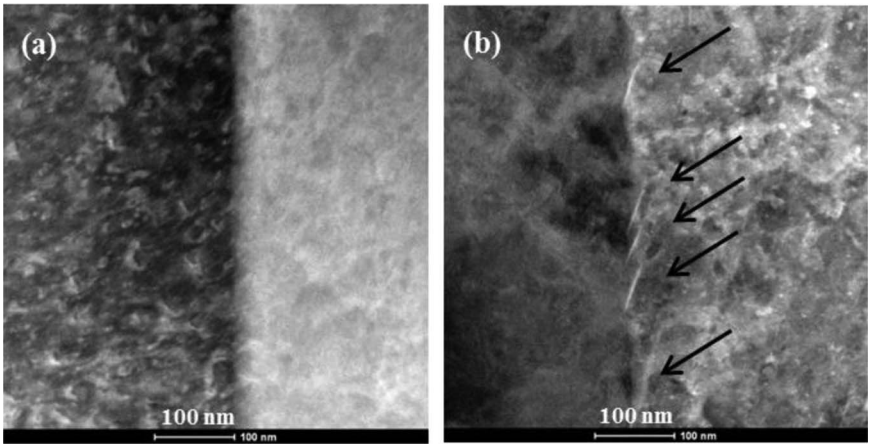

Figure 12. ADF STEM images of (a) a Σ and (b) a random grain-boundary. The arrows on (b) indicate the line shaped inclusions.

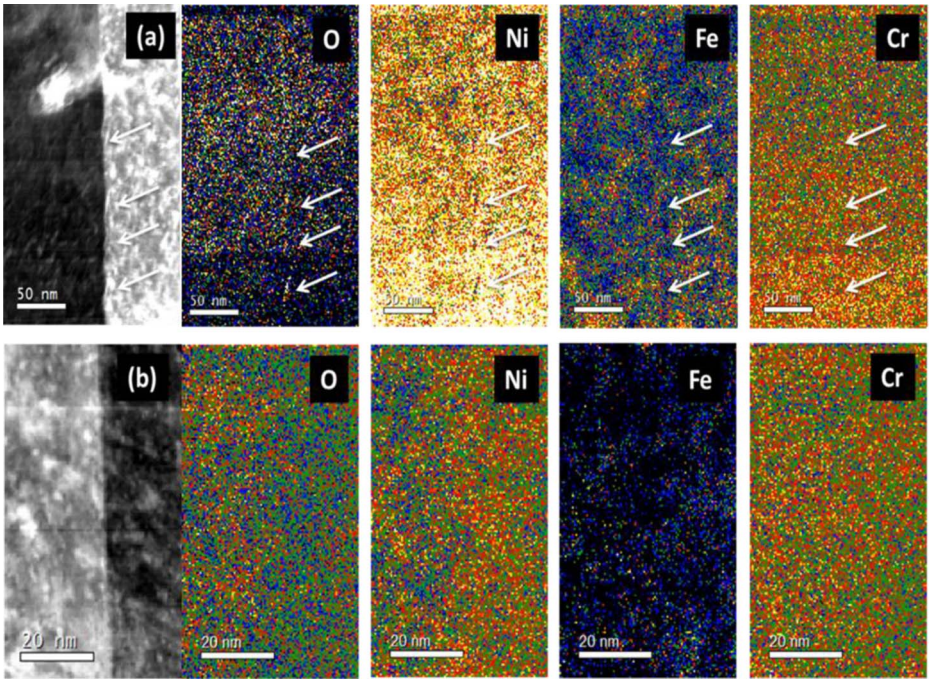

Figure 13. EELS maps of (a) a random, and (b) a Σ grain boundary and the related elemental composition maps of the same area on the TEM sample (Figure 12): the arrows show the location of needle-shaped inclusions.

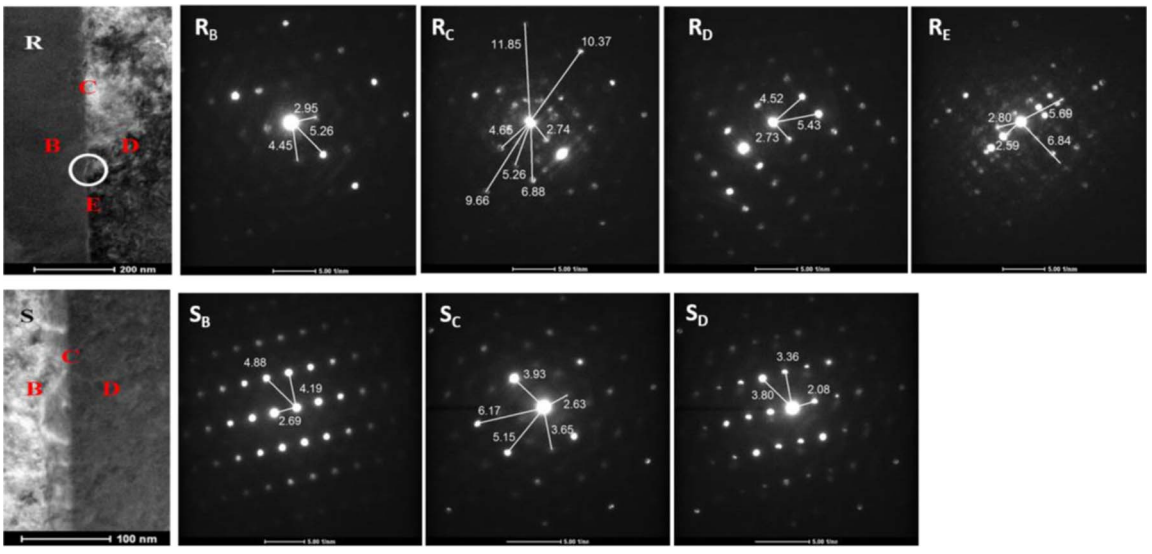

Figure 14. A Σ (S) and a random (R) grain boundary and the diffraction patterns of the two adjacent grains (B) and (D) and the grain boundaries (C) and the needle shape inclusion (E) on the TEM sample. The numbers on the diffraction patterns are the d spacing (1/nm) of the pattern.

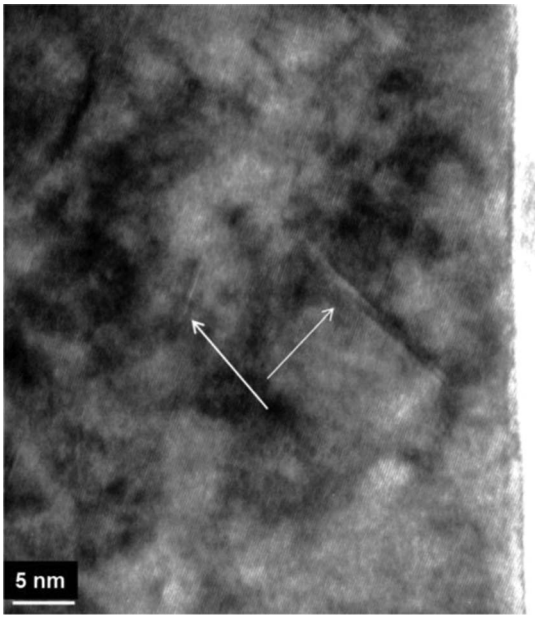

Figure 15. Line dislocation detected in the vicinity of random grain boundary of the TEM sample.

Acknowledgment

This research was supported by the Canadian Natural Sciences and Engineering Council (NSERC). The Nanofab facility at University of Western Ontario is acknowledged for use of their equipment. TEM research was performed at the Canadian Centre for Electron Microscopy at McMaster University, which is supported by NSERC and other government agencies. Haynes International (Kokomo, Indiana, USA) supplied the alloys.

References

1. Y. Gao, R. O. Ritchie, M. Kumar, and R. K. Nalla, *Metall. Mater. Trans. A*, **36**, 3325 (2005).
2. R. C. Reed, *The Superalloys: Fundamentals and Applications*, p. 372, Cambridge University Press, (2006).
3. J. R. Davis, *Nickel, Cobalt, and Their Alloys*, p. 442, ASM International, (2000).
4. T. M. Pollock and S. Tin, *J. Propuls. Power*, **22**, 361 (2006).
5. J. R. Hayes, J. J. Gray, A. W. Szmodis, and C. A. Orme, *Corrosion*, **62**, 491 (2006).
6. M. Moriya and M. B. Ives, *Corrosion*, **40**, 62 (1984).
7. A. K. Mishra, S. Ramamurthy, M. Biesinger, and D. W. Shoesmith, *Electrochim. Acta*, **100**, 118 (2013).
8. A. K. Mishra and D. W. Shoesmith, *Corrosion*, **70**, 721 (2014).
9. R. M. Carranza, C. M. Giordano, M. A. Rodríguez, and R. B. Rebak, *Corrosion/2008*, 0857, (Houston TX: NACE International 2008).
10. A. C. Lloyd, J. J. Noël, N. S. McIntyre, and D. W. Shoesmith, *JOM*, **57**, 31 (2005).
11. S. Haudet, M.. Rodríguez, R. M. Carranza, N. S. Meck, and R. B. Rebak, in *Corrosion2012*, NACE International (2012).
12. R. M. Carranza, M. A. Rodríguez, and R. B. Rebak, *Corrosion*, **63**, 480 (2007).
13. N. S. Zadorozne, C. M. Giordano, M. A. Rodríguez, R. M. Carranza, and R. B. Rebak, *Electrochim. Acta*, **76**, 94 (2012).
14. P. Jakupi, J. J. Noël, and D. W. Shoesmith, *Corros. Sci.*, **54**, 260 (2012).
15. P. Jakupi, J. J. Noel, and D. W. Shoesmith, *Corros. Sci.*, **53**, 3122 (2011).
16. P. Jakupi, F. Wang, J. J. Noël, and D. W. Shoesmith, *Corros. Sci.*, **53**, 1670 (2011).
17. N. Ebrahimi, P. Jakupi, J. J. Noel, and D. W. Shoesmith, *Corrosion*, **71**, 1441 (2015).
18. A. Mishra, X. Zhang, and D. Shoesmith, *Corrosion*, **In-Press** (2015).
19. N. Ebrahimi, J. J. Noël, M. A. Rodríguez, and D. W. Shoesmith, *Corros. Sci.*, In Press (2016).
20. P. Jakupi, J. J. Noël, and D. W. Shoesmith, *Electrochem. Solid-State Lett.*, **13**, C1 (2010).
21. M. Tang, W. C. Carter, and R. M. Cannon, *Phys. Rev. Lett.*, **97**, 75502 (2006).
22. D. L. Engelberg, in *Shreir's Corrosion*, p. 810, Elsevier (2010).
23. D.. G. Brandon, *Acta Metall.*, **14**, 1479 (1966).
24. G. Palumbo, E. M. Lehockey, and P. Lin, *JOM*, **50**, 40 (1998).
25. S. Kobayashi, T. Maruyama, S. Tsurekawa, and T. Watanabe, *Acta Mater.*, **60**, 6200 (2012).
26. C. a. Schuh, M. Kumar, and W. E. King, *Acta Mater.*, **51**, 687 (2003).
27. L. Tan, X. Ren, K. Sridharan, and T. R. Allen, *Corros. Sci.*, **50**, 3056 (2008).
28. V. Randle, P. R. Rios, and Y. Hu, *Scr. Mater.*, **58**, 130 (2008).
29. L.. Lim and R. Raj, *Acta Metall.*, **32**, 1177 (1984).
30. M. A. Tschopp and D. L. McDowell, *Philos. Mag.*, **87**, 3147 (2007).
31. M. A. Arafin and J. A. Szpunar, *Corros. Sci.*, **51**, 119 (2009).
32. E. M. Lehockey and G. Palumbo, *Mater. Sci. Eng. A*, **237**, 168 (1997).
33. Y. Gao, J. S. Stölken, M. Kumar, and R. O. Ritchie, *Acta Mater.*, **55**, 3155 (2007).
34. C. Luo, X. Zhou, G. E. Thompson, and A. E. Hughes, *Corros. Sci.*, **61**, 35 (2012).
35. V. Randle, *Mater. Charact.*, **60**, 913 (2009).
36. I. Saxl, A. Kalousová, L. Ilucová, and V. Sklenička, *Mater. Charact.*, **60**, 1163 (2009).
37. ASTM Standard E112, *Standard Test Methods for Determining Average Grain Size*, (2012).
38. R. S. Lillard, M. P. Jurinski, and J. R. Scully, *Corrosion*, **50**, 251 (1994).
39. D. J. Horton, A. W. Zhu, J. R. Scully, and M. Neurock, *MRS Commun.*, **4**, 1 (2014).
40. J. J. Gray, B. S. El Dasher, and C. A. Orme, *Surf. Sci.*, **600**, 2488 (2006).
41. R. Rapp, *Acta Metall.*, **9**, 730 (1961).
42. T. S. Gendron and R. C. Newman, in *CORROSION1994*, p. paper No.181., NACE International, Houston, TX (1994).
43. S. Y. Persaud, A. Korinek, J. Huang, G. A. Botton, and R. C. Newman, *Corros. Sci.*, **86**, 108 (2014).
44. J. Li, S. J. Dillon, and G. S. Rohrer. *Acta Mater*, **57**, 4304 (2009).
45. D. L. Olmsted, S. M. Foiles, and E. A. Holm, *Acta Mater*, **57**, 3694 (2009).